

Supporting Information for:

Modelling the risk of deterioration at earthen heritage sites in drylands

**Jenny Richards¹, Jerome Mayaud¹, Hongtao Zhan², Fasi Wu², Richard Bailey¹,
Heather Viles¹**

¹ School of Geography and the Environment, University of Oxford, Oxford OX1 3QY,
UK.

² Dunhuang Academy, Dunhuang, 736200, China.

Introduction

This Supporting Information provides additional material to support the development of the Vegetation and Sediment TrAnsport model for Heritage Deterioration (ViSTA-HD). It presents the data used to inform parameterizations in ViSTA-HD as well as additional verification tests for both the environmental and deterioration modules.

S1. Field data used in parameterizing ViSTA-HD

Environmental data collected at Suoyang Ancient City were used to parameterize processes in ViSTA-HD's environmental and deterioration modules. Where relevant, data collected at Suoyang were combined with the datasets originally used to build ViSTA (Mayaud et al., 2017).

S1.1 Parameterizing the environmental module

S1.1.1 Seasonality of climate at Suoyang

Wind velocity was recorded at Suoyang between September 2015 and August 2016 using an automatic weather station (Figure S1). The climate at Suoyang has strong seasonal patterns with strong easterly winds dominating in summer and weak westerlies and south-easterlies dominating in winter. This strong seasonality was used to justify setting the temporal scale of each iteration to 3 months.

S1.1.2 Wind velocity recovery

In Mayaud et al.'s (2017a) validation of wind recovery in the lee of vegetation elements in the Kalahari, they did not use data from elements with a porosity less than 30%. Preliminary optical porosity tests undertaken at Suoyang. Results showed that whilst the dominant vegetation species had similar structural features to those used to parameterize ViSTA, the range of porosities at Suoyang was significantly greater than in the Kalahari, with some plants having optical porosities as low as 2%. To capture a fuller range of wind recovery distances, wind velocity data from around low-porosity elements in Suoyang were combined with Mayaud et al.'s (2017a) original dataset. This combined dataset was used to parameterize wind flow in ViSTA-HD.

Using the methodology described in the open-source methodology of Mayaud et al. (2017a), we used the combined Kalahari-Suoyang dataset to determine the parameterisation of the mean normalized wind velocity (u_0) at 1 h downwind of the vegetation element (where h is the height of the plant) as:

42
$$u_0 = 0.0002p^2 - 0.0117p + 0.3345$$

43 (Equation S1)

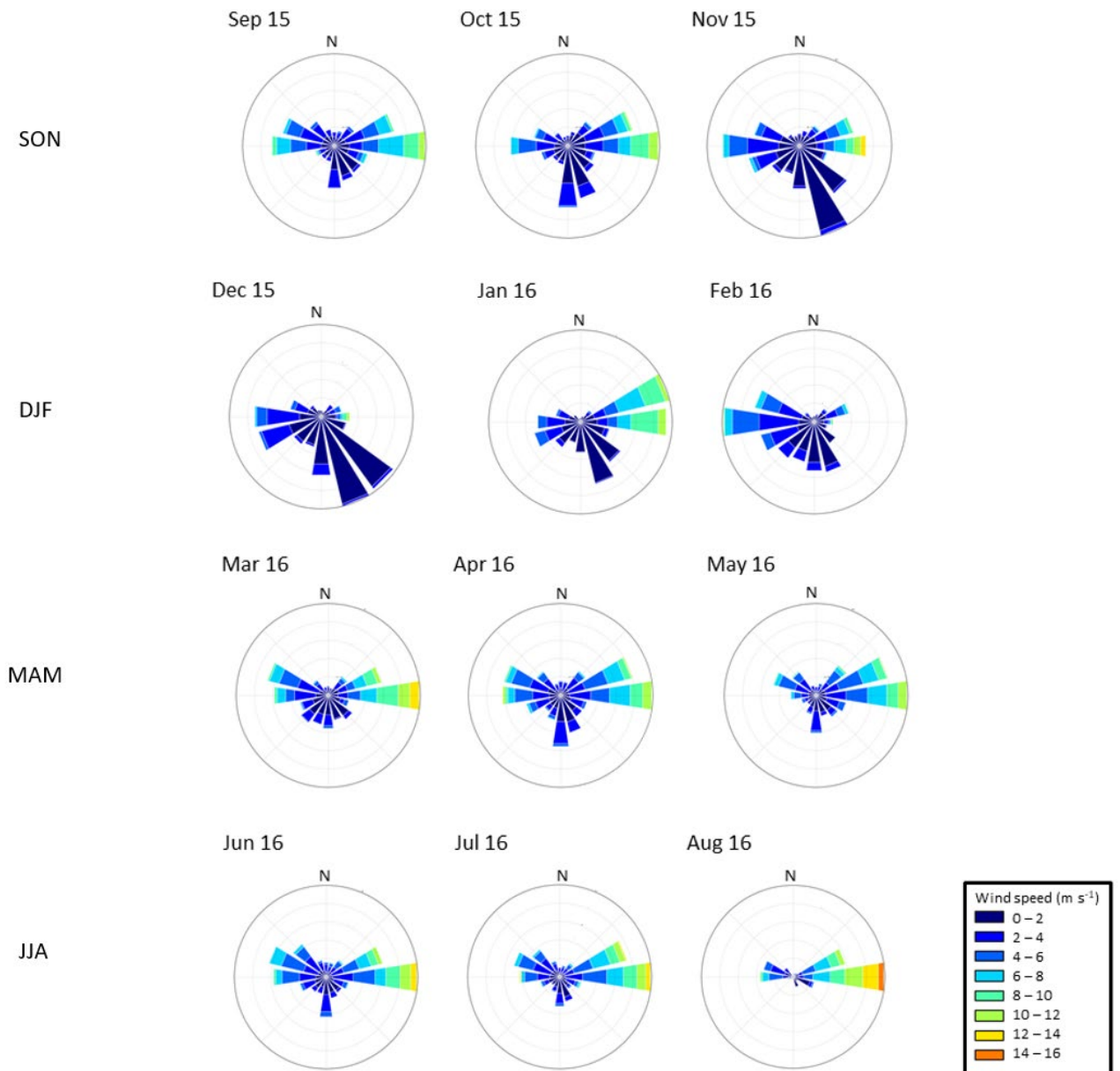
44 And the rate of wind recovery in the lee of the vegetation, determined by the b
 45 coefficient, as:

46
$$b = \begin{cases} 0.32 & (p < 65\%) \\ 0.65 & (p \geq 65\%) \end{cases}$$

47 (Equation S2)

48 where p is the porosity of the vegetation element (Figure S2).

49 Bayesian selection criteria is a criterion for selecting between a finite set of
 50 models that determines the optimum number of parameters within the model, without
 51 overfitting. We applied this criterion to our wind recovery data in Microsoft Excel to
 52 select the wind recovery model used in ViSTA-HD.



53

54 **Figure S1:** Wind velocity recorded at Suoyang between September 2015 and
 55 August 2016, grouped into four seasons.

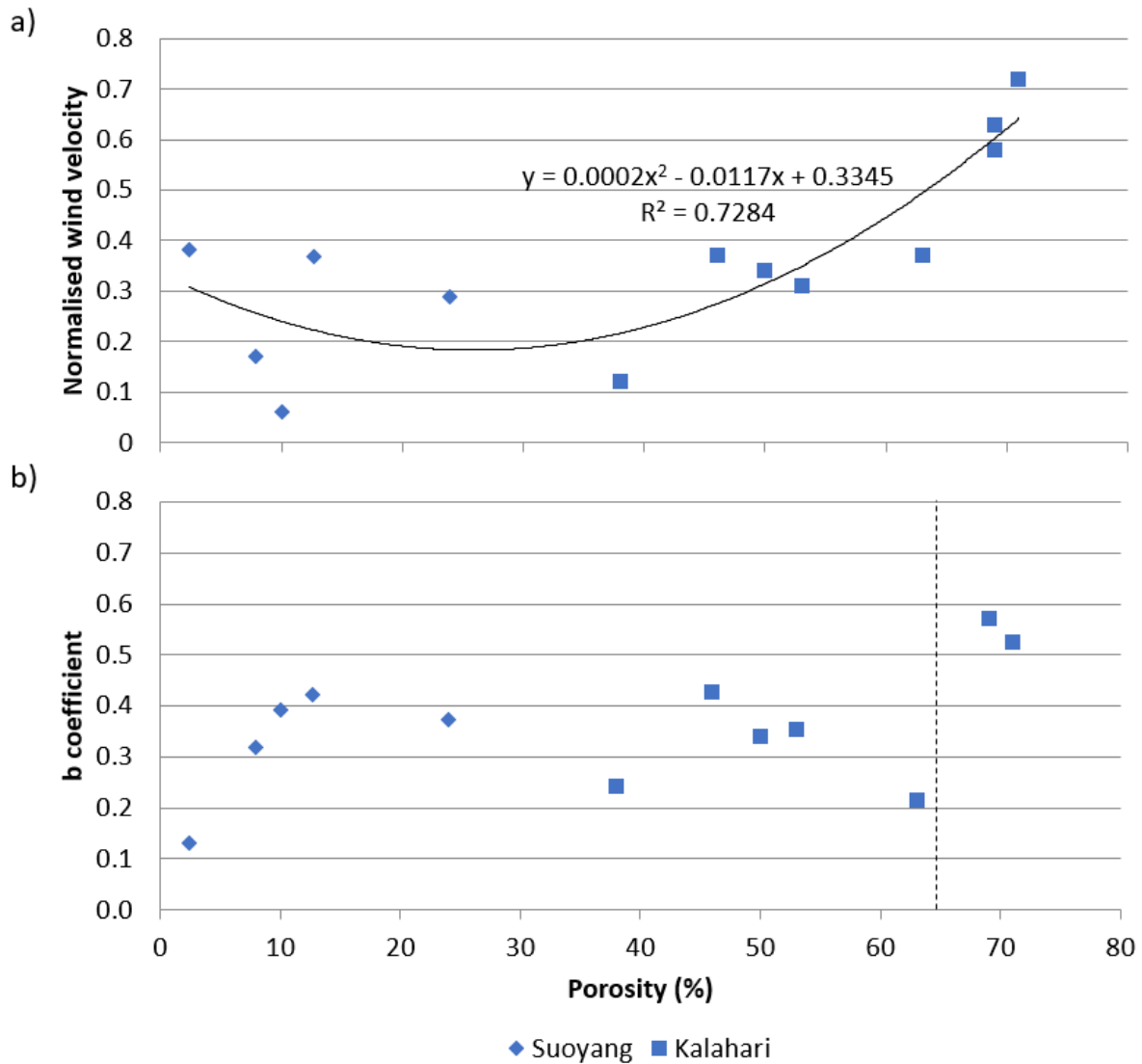


Figure S2: The relationship between porosity and **a)** the mean normalized minimum wind velocity, and **b)** the b coefficient using the joint Kalahari-Suoyang dataset.

S1.1.3 Wind flow round earthen walls

Solid structures, such as earthen walls, alter wind flow (Richards et al., 2001; Tsoar, 1983). To understand the impact of earthen heritage on wind flow, wind velocity measurements were taken 50 cm above the ground around the Suoyang test walls. The measurements showed that the extent to which the wind was laterally accelerated around the walls was strongly dependent on the location of the wall to

other walls and the approach angle of the wind (Figure S3). When the wind flow was travelling between two walls, the lateral acceleration was notably greater than when it was travelling around a wall edge that did not have another wall within 2 m, owing to airflow compression (Garvey et al., 2005; Richards et al., 2001). The acceleration was greatest when the wind direction was perpendicular to the wall (0°) and decreased linearly as the wind direction became more acute to the wall face (Figure S3). These linear regressions were used to parameterize the acceleration of wind velocity around the walls in ViSTA-HD.

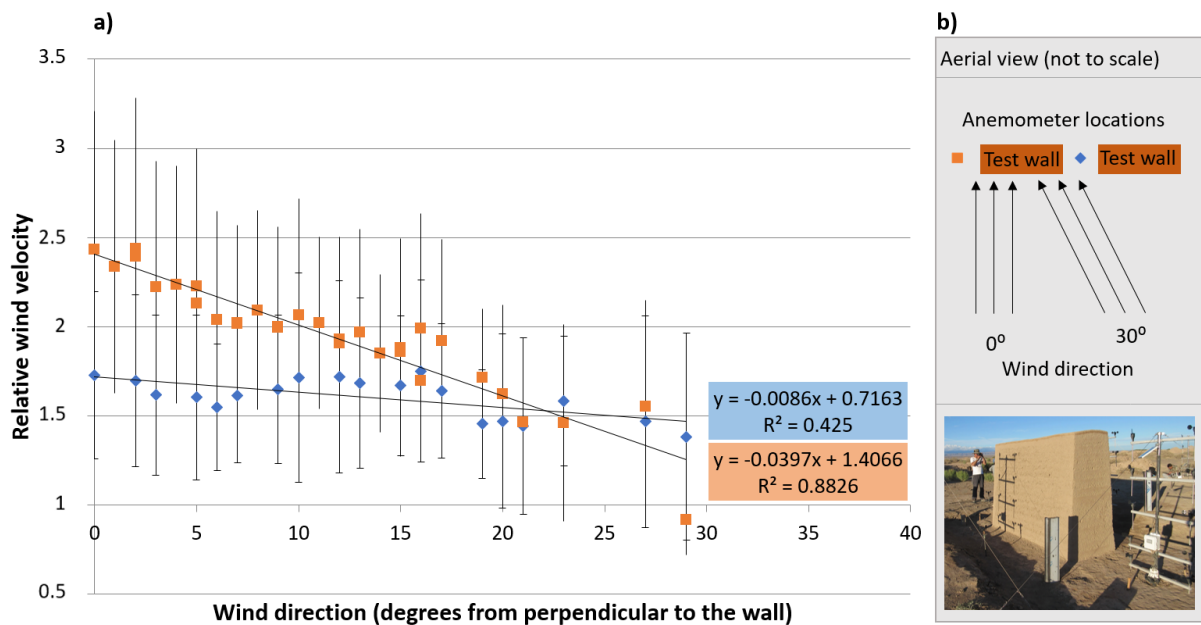


Figure S3: a) The relationship between wind direction and relative wind velocity at two locations shown in **b)**. The relative wind velocity is calculated according to the wind velocity at 1 h upwind of the wall (where h is the height of the wall).

S1.1.4 Sediment transport

The presence of solid structures also affects sediment transport. Unlike plants, where their lower porosity enables some sediment to travel through the element

(Mayaud et al., 2017), solid objects can act as a trap, resulting in the formation of dunes in front of such objects (Rowell et al., 2018; Tyson, 1999).

In ViSTA-HD, sediment transport pathways are always modelled as following the simulated wind direction, because sediment transport does tend to align with wind direction in field studies (omitting small-scale processes such as sand snakes and minor recirculation zones) (Anderson et al., 1991; Gares et al., 1996; Goossens and Offer, 2000; Sherman and Hotta, 1990). Tests using smoke flares around the test walls at Suoyang revealed that wind flow gets deflected around wall faces (Figure S4), so in the model, sediment transport pathways that come into contact with wall faces are deflected sideways accordingly.

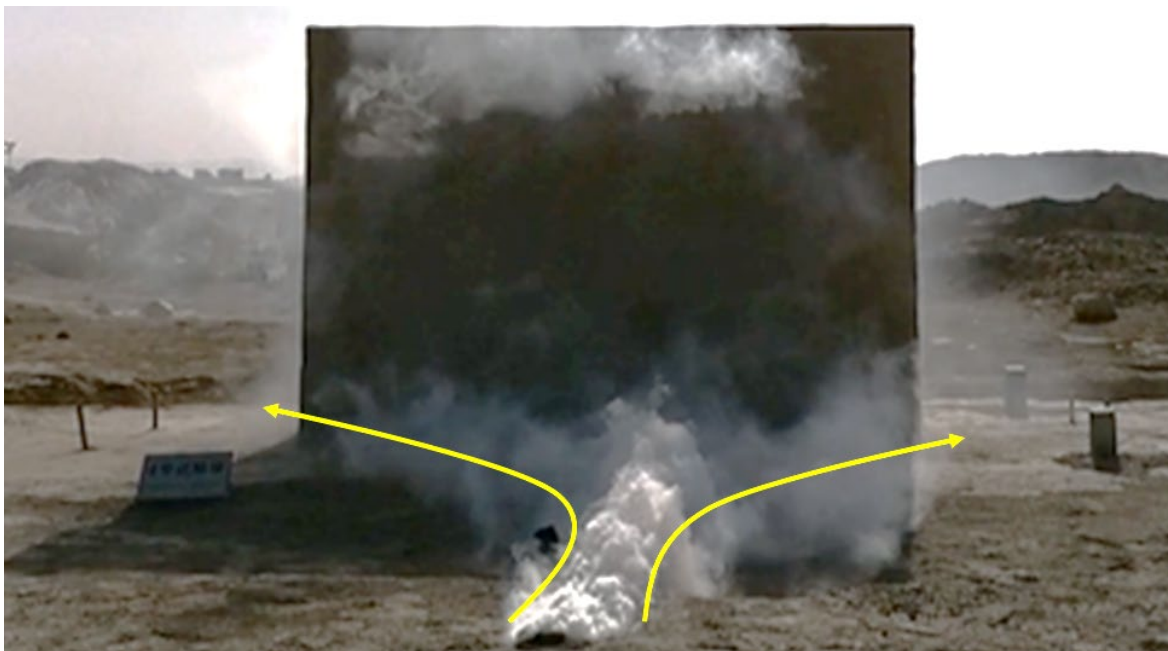


Figure S4: A photograph of the flare experiment showing the deflection of the wind flow around the test wall.

94 S1.2 Parameterizing the deterioration module

95 Environmental data from Suoyang was also used to inform the environmental
96 conditions occurring across the wall face in the deterioration module. As wind
97 velocity is resolved at 050 cm above the surface, the wind velocity determined by the
98 environmental modules is imputed into the deterioration module at 50 cm above the
99 surface. Due to the different cell resolutions in the environmental (1 m) and
100 deterioration (0.25 m) modules, the inputs from the environmental module are
101 inputted into deterioration module cells which align centrally with the environmental
102 module cells (Figure S5). Conditions at 50 cm above the surface are linearly
103 interpolated where appropriate (see Figure S5b for example).

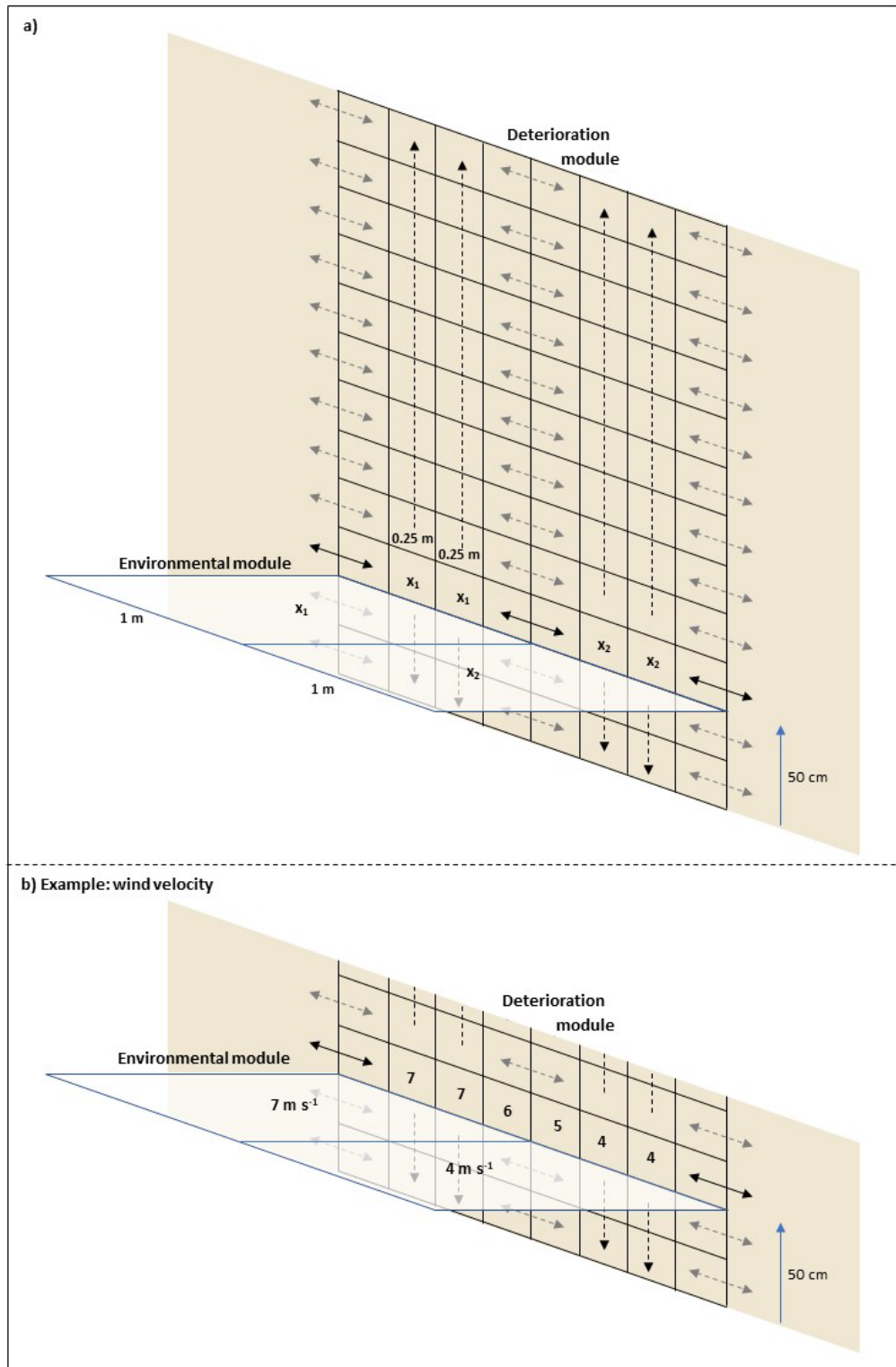


Figure S5: a) The interaction of the environmental and deterioration modules at the wall face: x_1 and x_2 represent environmental conditions resolved in the environmental module. The solid black arrows show interpolation between inputs. Dashed vertical arrows indicate the extrapolation of conditions above and below the environmental

input and the dashed horizontal arrows indicate the interpolation between calculated conditions across the wall face. **b)** An example of wind velocity inputs from the environmental module into the deterioration module.

Wind towers located 0.5 m away from the test wall, with cup anemometers located at 0.2, 0.5, 1, 1.5 and 2 m above the ground, were used to determine how wind speed changed with height up the wall face (Figure S6a). As the historic walls at Suoyang can be much taller than the 2 m test wall, the dataset was fitted with an exponential curve, such that the rate of increase in wind velocity decreased with height.

A wedge-shaped sediment trap (90 cm tall made up of 2 cm increments) located 1 m upwind of the test wall was used to determine how sediment transport varies with height. The trap was deployed for one month after which the mass of sediment in each increment was measured in the laboratory using an Ohaus mass balance with 0.01 g precision (Figure S6b). We observed that sediment volume decreased with height between 0 and 40 cm above the surface, above which the volume of sediment remained constant at all heights. We therefore consider the saltation zone to occur within the first 40 cm above the surface, similar to Dupont et al. (2013) (as shown by the dashed line in Figure S6b).

These parameterized environmental conditions across the wall face were used to inform the environmental risk of polishing, pitting and slurry across the wall face (see Figure 5 in the main paper for further details).

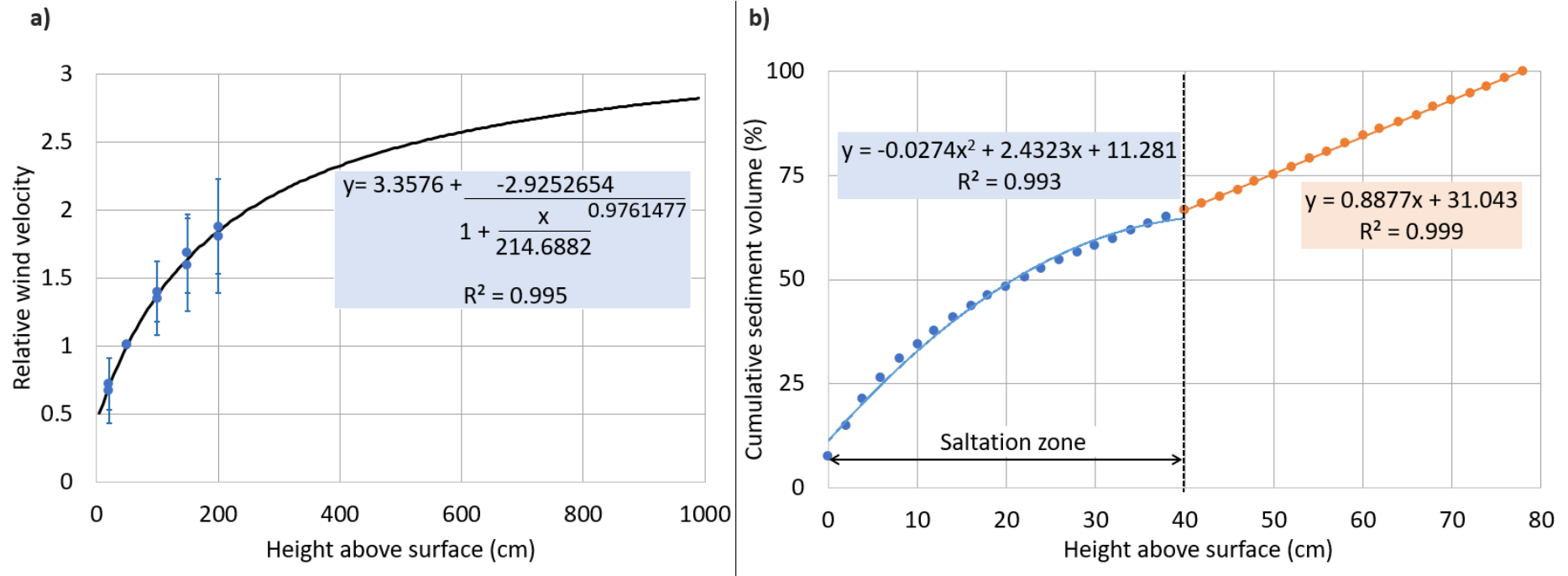


Figure S6: Change in **a)** wind velocity (relative to the wind velocity 0.5 m above the ground), and **b)** total volume of transported sediment, with increasing height from the ground. The dashed black line in **b)** indicates the determined height for sediment transport occurring within and above the saltation zone.

S2. Model verification

S2.1 Environmental module

S2.1.1 Climatic inputs

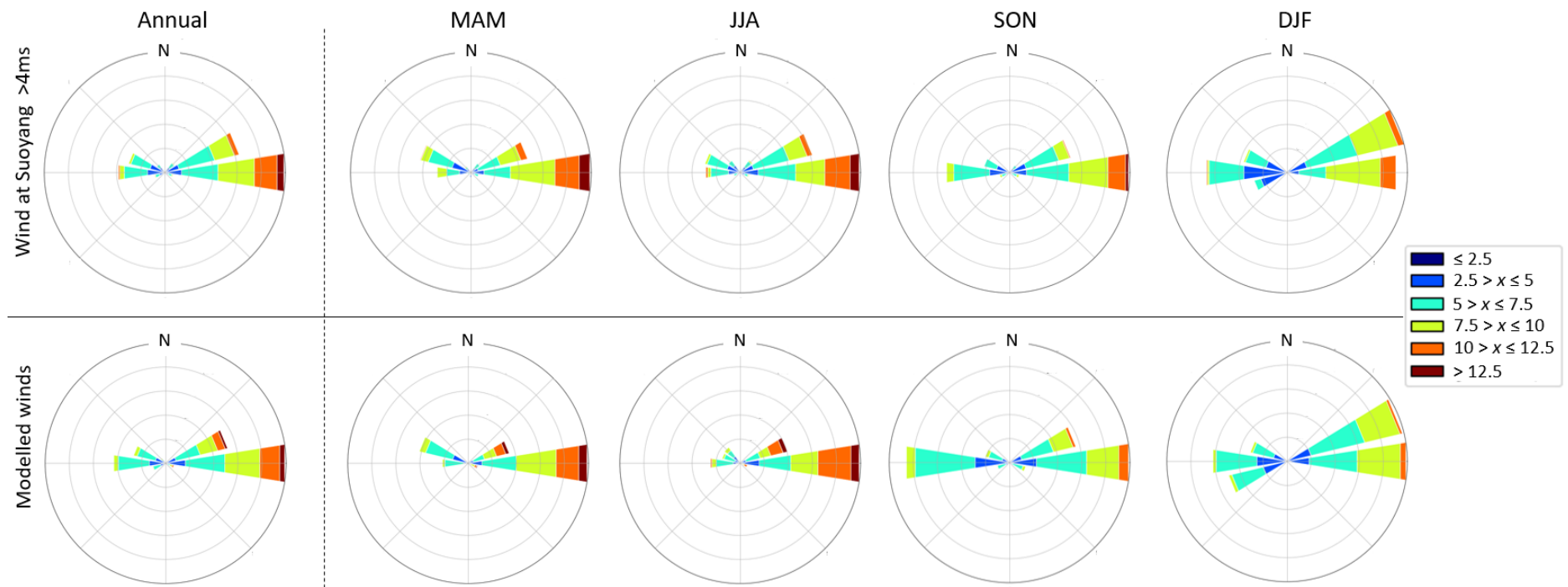
Environmental and deterioration processes within ViSTA-HD are driven by wind velocity, sediment availability and rainfall.

Wind velocity data (shown in Figure S1) was used to inform the wind regime inputted into ViSTA-HD. Since low wind velocities are unlikely to pose a deterioration risk, rarely entrain sediment (Dong et al., 2003), and are commonly interspersed with greater gusts of wind, we disregarded periods in the dataset when wind velocities dropped below 4 m s^{-1} . We used the remaining data to derive seasonal probability density functions that drive wind velocity the environmental module. In each iteration, a wind velocity was randomly selected from the probability density function to provide an unobstructed wind velocity (u_{ref}) that represents the mean flow over flat surfaces. The unobstructed wind velocity was held constant for the duration of each iteration. To capture the stochastic nature of airflow, a stochasticity function developed by Mayaud et al. (2017a) was applied to wind flow in ViSTA-HD enabling variation in wind velocities between identical cells (see Mayaud et al. 2017a for description).

After running ViSTA-HD for 200 iterations, the modelled wind velocities were visually compared to the wind velocities recorded at Suoyang (Figure S7). There was good agreement between the modelled and recorded wind velocities. The seasonal variations were captured with, for example, the strongest winds occurring in the

summer and westerlies becoming more dominant in autumn and winter (Figure S7). This enables the environmental processes modelled within ViSTA-HD to be reflective of those occurring at Suoyang over both annual and seasonal timescales.

Historic rainfall data provided by the Dunhuang Academy showed that between 1986 and 2005, the average annual precipitation was 49.2 mm, ranging between 33.6 mm and 74.2 mm. The average seasonal rainfall over this period was 6 mm, 12 mm, 25 mm and 6 mm for winter, spring, summer and autumn respectively. The maximum recorded daily rainfall in this period was 30.7 mm. In addition, a limited rainfall dataset collected at the site between March and December 2018 was also used to inform the frequency of rainfall events. This data was used to parameterize the rainfall within ViSTA-HD (Figure S8)



168

169 **Figure S7:** Wind roses comparing the wind regime above 4 ms⁻¹ at Suoyang to the wind velocities inputted into ViSTA-HD.

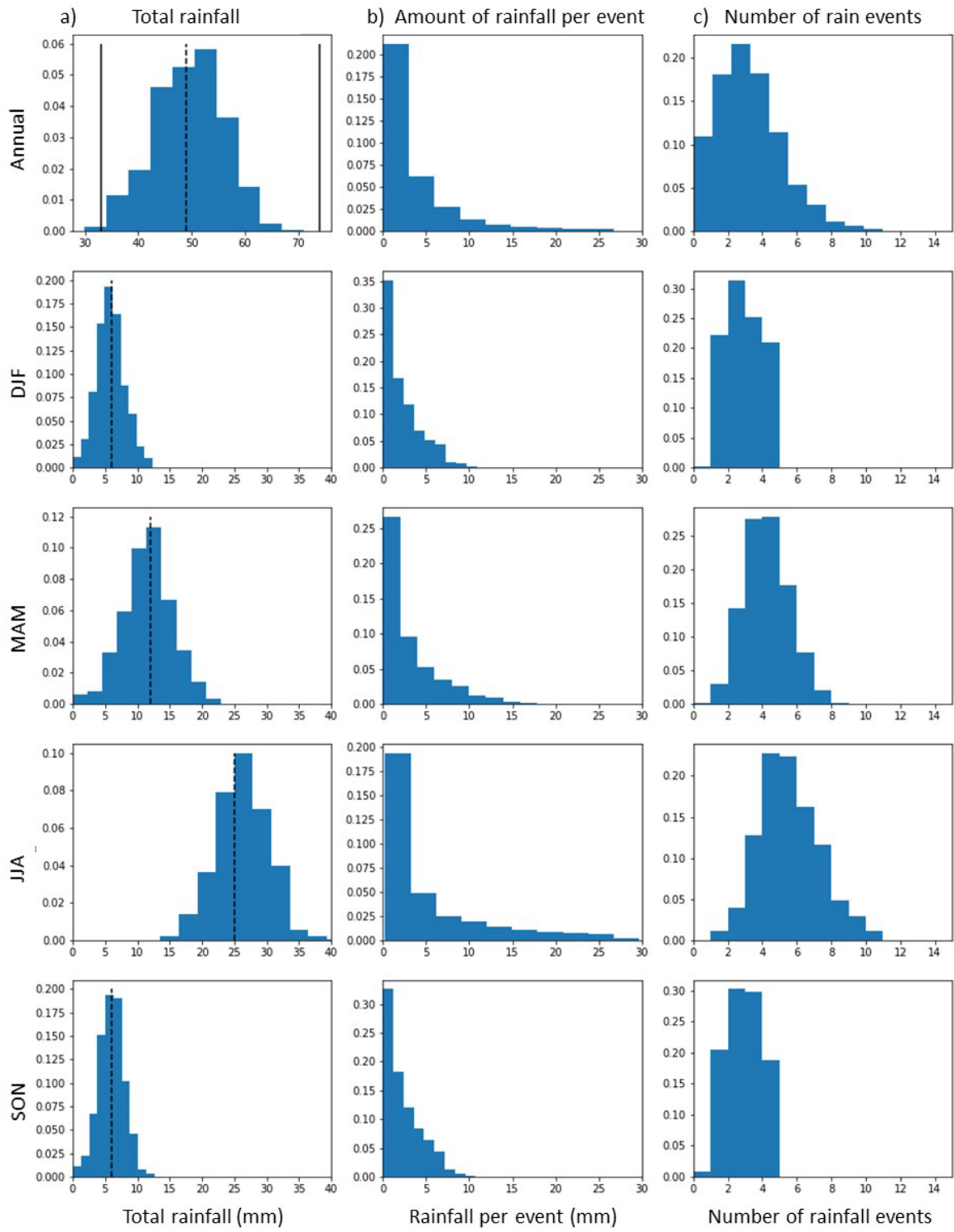


Figure S8: a) Total rainfall, **b)** quantity of rainfall in each storm event, and **c)** the number of rain events per iteration, over an annual time period and for each season (DJF, MAM, JJA, SON) individually. The dashed black lines in the first panel show

the mean annual rainfall and the solid black lines shown the minimum and maximum annual rainfall.

S2.1.2 Wind flow dynamics

Laboratory studies (Tsoar, 1983) and results from Suoyang found that wind velocity begins to decelerate at $3h$ (where h is the height of the wall) upwind of a wall. In addition, lateral acceleration around the walls was observed at Suoyang (Figure S3) and wind velocities downwind of the wall recovered within $15h$. ViSTA-HD is able to capture these interactions between earthen walls and wind flow, with taller walls having longer upwind turbulence zones as well as a longer downwind shadow zones (Figure S9).

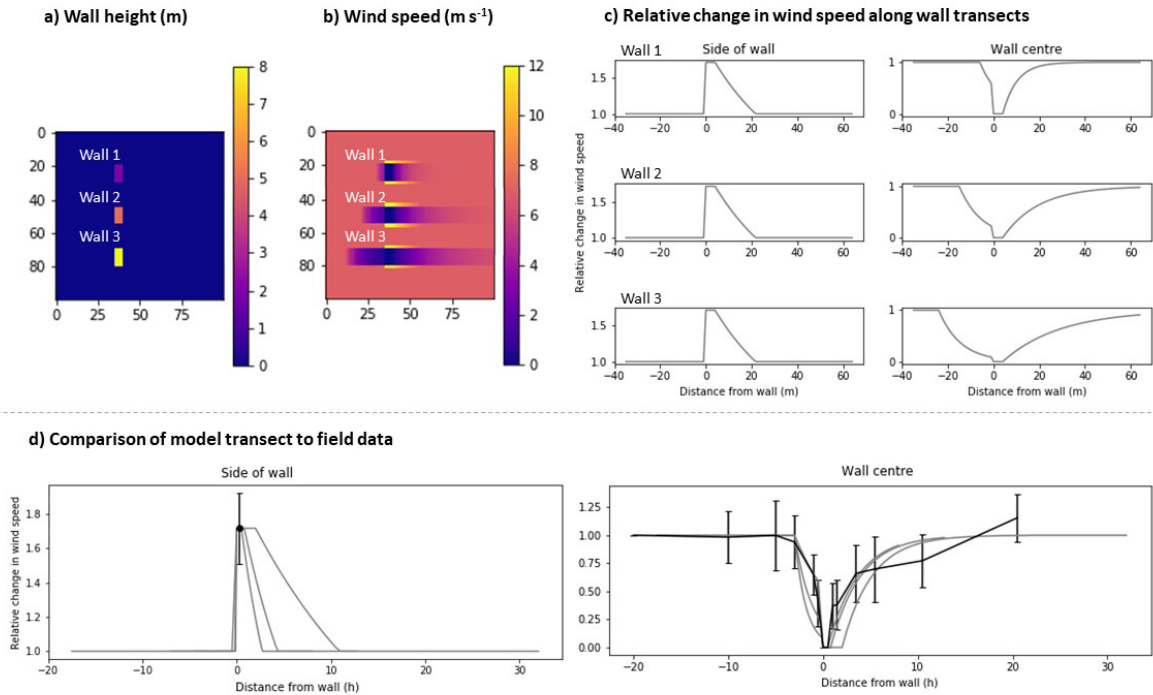


Figure S9: A comparison of the modelled wind flow around three walls of different heights (3, 5 and 8 m) with data collected from Suoyang: **a)** Location and heights of the three modelled walls; **b)** wind velocity across the model space caused by a wind blowing from left to right; **c)** transects of wind velocity to the side of the wall where acceleration occurs and through the centre of the wall; **d)** comparison of modelled wind velocities (grey) to wind velocities collected at Suoyang (black). The distance from wall is reported in h (where h is the height of the wall), to enable comparison between model and field data. Error bars show one standard deviation from the mean.

S2.1.3 Sediment transport

At Suoyang, earthen walls can act as a sediment trap allowing the development of dunes around the walls. To verify that the walls present within ViSTA-HD were able to act as a sediment trap, the model was run for 300 iterations, with 1.5 m of

sediment in all grid cells and no vegetation coverage, with winds alternating west-north-west and west-south-west. Dune features developed in front of both the long and short walls (Figure S10). It is notable that the dune in front of the longer wall was more persistent, which reflects dunes observed at Suoyang where sediment is transported around shorter wall sections.

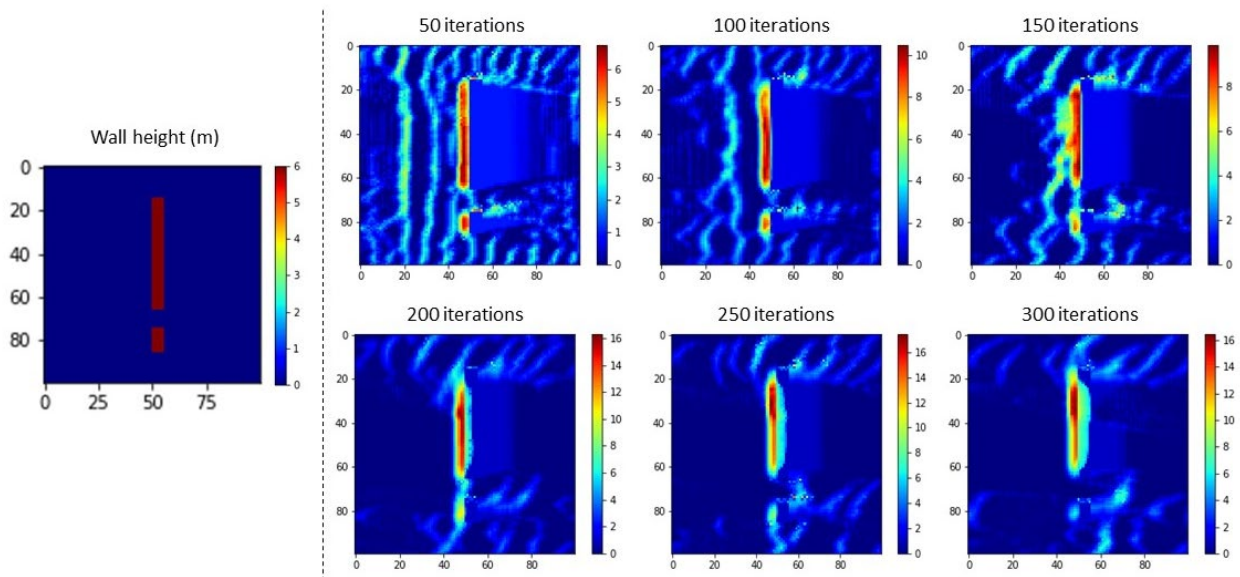


Figure S10: The development of dunes in front of two walls (measuring 50 m and 10 m in length and 6 m in height), over 300 iterations.

S2.1.4 Dune dynamics

To further verify the development of dunes within ViSTA-HD, the morphology of modelled dunes was compared to those found at Suoyang in four different model setups: (i) two short walls (10 m in length) located close together; (ii) a long wall (40 m) and a short wall (10 m); (iii) two long walls (80 m) with one placed downwind of the other; (iv) and a long wall (40 m) and a short wall (10 m) with 80% vegetation cover (Figure S11). Dune morphology was assessed using measurements that could

be taken both in the model and in the field. The height of the exposed wall face and the length of the dune on the upwind side of the wall were compared at the end of each model run.

Each model setup was initially inputted with environmental conditions reflective of seasonal variations observed at Suoyang (Figure S7Figure S8). Each model setup was run for 500 iterations (representing 125 years in real time) and repeated 10 times. Proportional histograms were created to display the range in the height of the exposed wall face and the length of the modelled dunes (Figure S11). The measurements taken from the dunes at Suoyang were categorized by wall length (short walls < 10 m, long walls > 10 m) and vegetation (<70%, > 70% vegetation coverage) and were overlain on the modelled results with black triangles (Figure S11).

The height of exposed wall for the modelled dunes corresponded well with the dunes measured at Suoyang, except for dunes located in front of the long walls. The development of the dunes in front of the two long walls was limited by the total number of iterations run in this experiment, which suggests that dunes in the field are likely to have developed over a longer period of time than represented by the model run. For all set up conditions, the model runs did not capture the longer dune lengths. The lack of shorter dune measurements may have been influenced by a sampling bias in the field, as we only chose to sample walls which had notable upwind dunes. The dune lengths may also be influenced by varying climate regimes that are not captured within the model. Nevertheless, the modelled dune lengths are generally within 1 or 2 h of the dune lengths measured in the field, which we consider acceptable for the purposes of this model.

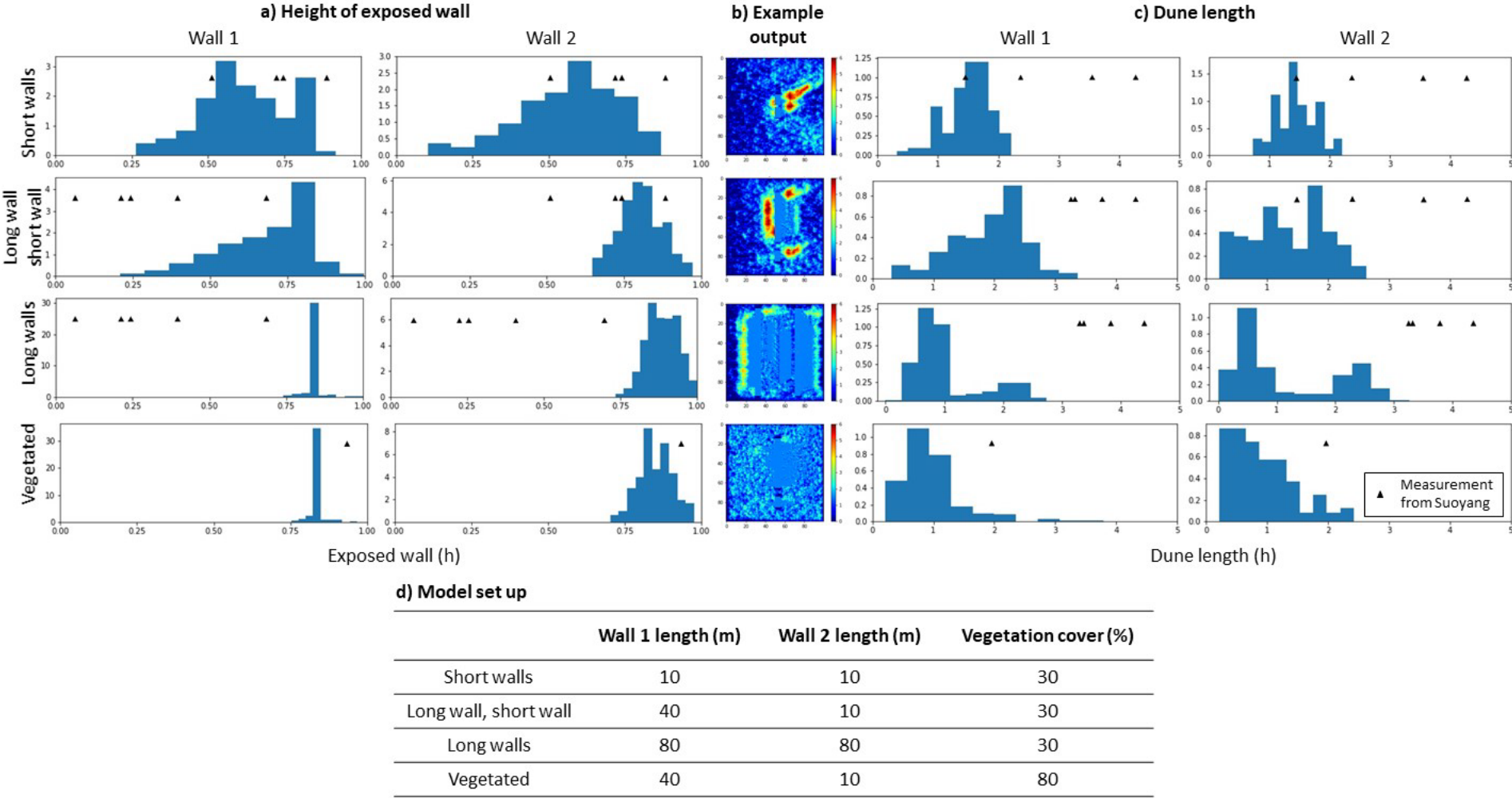
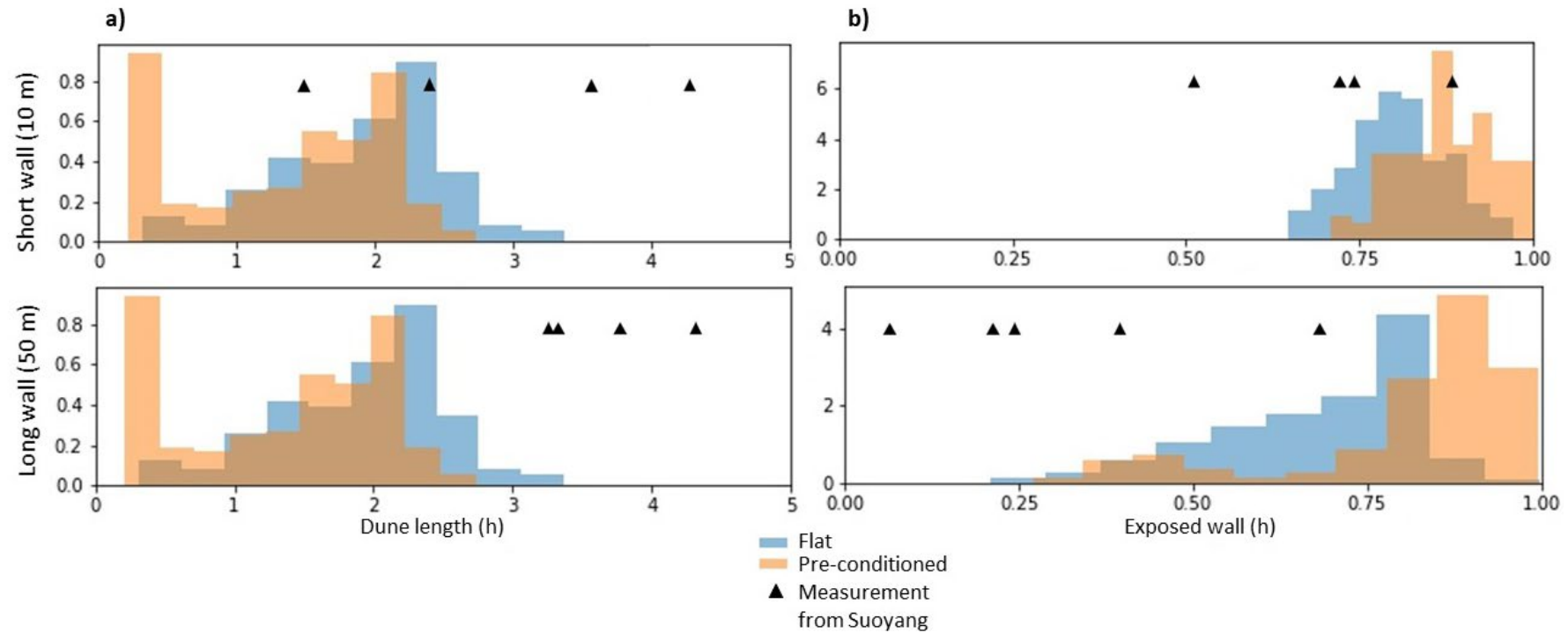


Figure S11: Comparison of modelled and real dune morphologies on the upwind side of walls. The range of dunes morphologies are shown using histograms for the modelled dunes and triangles for the measurements taken in the field. Four model

242 configurations were used to compare **a)** the height of exposed walls and **c)** the dune length. An example of each model
243 configuration after 500 iterations is shown in **b)**. The model set up is shown in **d)**.

Given that desert surfaces are rarely truly flat, the sensitivity of sediment build-up to surface topography was tested in ViSTA-HD. We used the same wall configuration as presented Figure S10, and two model setups were compared: one with an initial uniform 1.5 m layer of sediment, and the other with a pre-conditioned surface. The pre-conditioned surface was initialized by running the model for 500 iterations, removing the dune formations before the walls, and then equally distributing this sediment across the entire model space. For both the uniform and pre-conditioned starting setup, ViSTA HD was run 10 times for 500 iterations and the height of the exposed walls and length of dune for the upwind side of the wall were calculated (Figure S12).

On the flat model runs, the uniform distribution of sediment covered the lower 1.5 m section of the wall, whereas this layer had been removed in the pre-conditioned, resulting in a greater proportion of the wall surface being exposed (although the similar distribution shapes suggests the difference between setups may not be significant). Similarly, the dune length distribution was similar between model runs, except for the prevalence of short dunes in the pre-conditioned model runs. This is also caused by the removal of sediment in front of the walls. Therefore, given the similarities between the model runs, it is not thought to make a significant difference if the model is inputted with uniform or pre-conditioned starting sand heights.



264

265 **Figure S12:** Comparison of dune morphologies between models starting with a uniform (flat) sand height and a pre-conditioned

266 surface for **a)** dune length and **b)** exposed wall where h is the height of the wall.

S2.2 Deterioration module

S2.2.1 Rainfall impact

In-situ observations have shown that rainfall impacts entire wall faces at Suoyang: after storm events, entire wind-facing wall faces are damp (Figure S13a) and entire wall face are marked by wind-driven slurry features (Figure S13b). Therefore, in ViSTA-HD wind-driven rain was parameterized as occurring equally across the wall face.



Figure S13: The impact of rain on **a)** test wall 24 hours after a storm event, and **b)** on the historic walls

S2.2.2 Setup for sensitivity tests

To test the inherent variability of the deterioration module, the module was run multiple times with the same initial conditions until the mean and standard deviation of overall deterioration from the model runs had stabilized. Once the mean and standard deviation of the model runs has stabilized this suggests that additional model runs will not significantly alter the result. The mean and standard deviation of

283 the overall deterioration for (i) the entire wall face and (ii) randomly selected
284 individual cells was calculated (Figure S14). The mean and standard deviations for
285 both the entire wall face and individual cells stabilized after approximately 50
286 replicate model runs. Consequently, the environmental module should be run for a
287 minimum of 50 repeats for each set of input conditions.

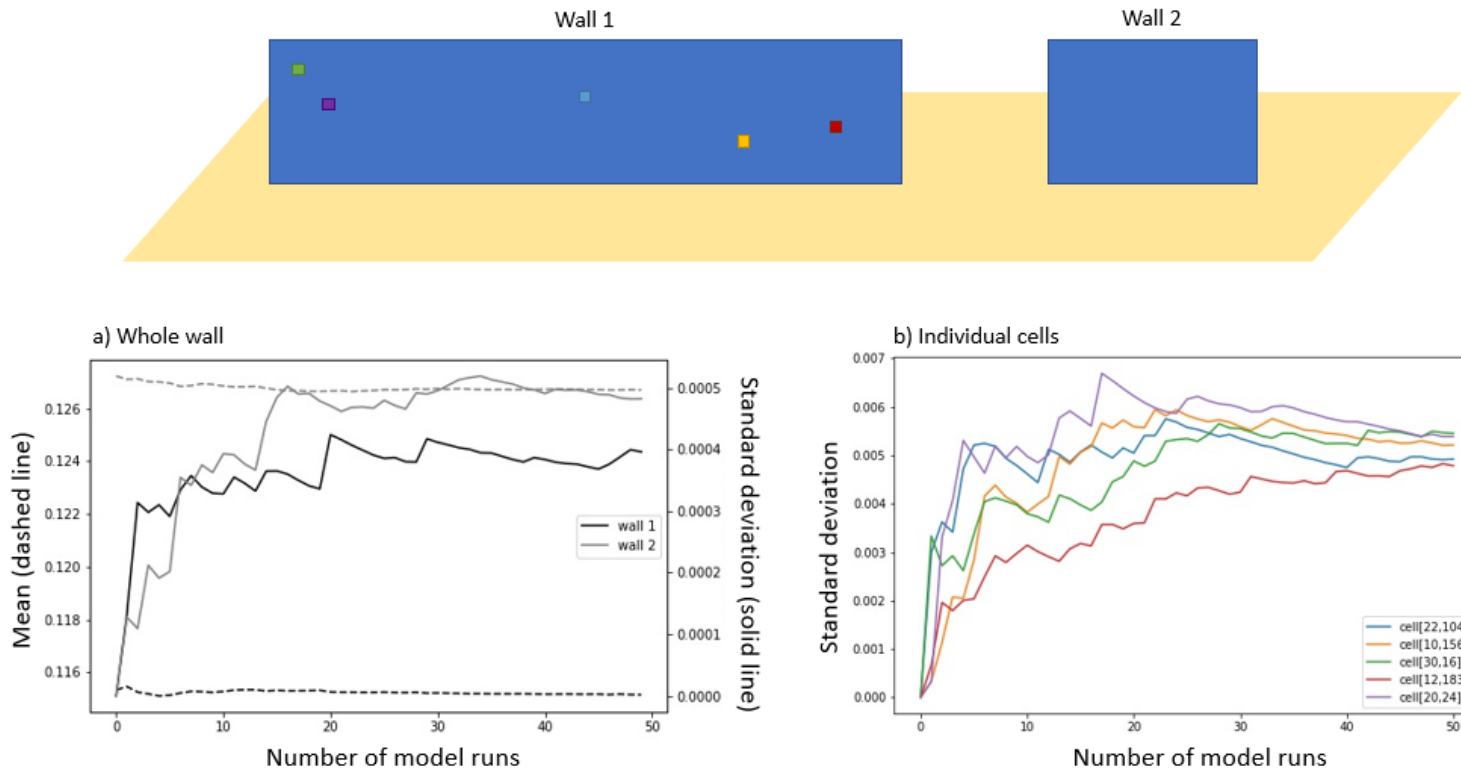


Figure S14: The running mean for 50 repeat runs of the **a)** mean and standard deviation of the risk of deterioration across two wall faces and **b)** the standard deviation of the risk of deterioration in randomly selected individual cells. The approximate location of the individual cells are shown on wall 1.

293 S2.2.3 *Spatial scale*

294 The spatial resolution of deterioration risk is constrained by the interpolation
295 required between the deterioration and environmental module (due to different
296 cell resolutions) and available computational power. With a resolution 0.02 m²
297 the deterioration module is able to resolve the reduced risk of deterioration
298 associated with compaction layers – seen in Figure S15 with the evenly
299 distributed stripes of reduced deterioration risk (Li et al., 2011; Shao et al., 2013).
300 However, due to the high computational burden required, it was only feasible to
301 model a 2.5 m section of the wall. Therefore, a resolution of 0.25 x 0.25 m was
302 chosen for the deterioration module to balance computational expense with
303 capturing smaller scale deterioration features.

304

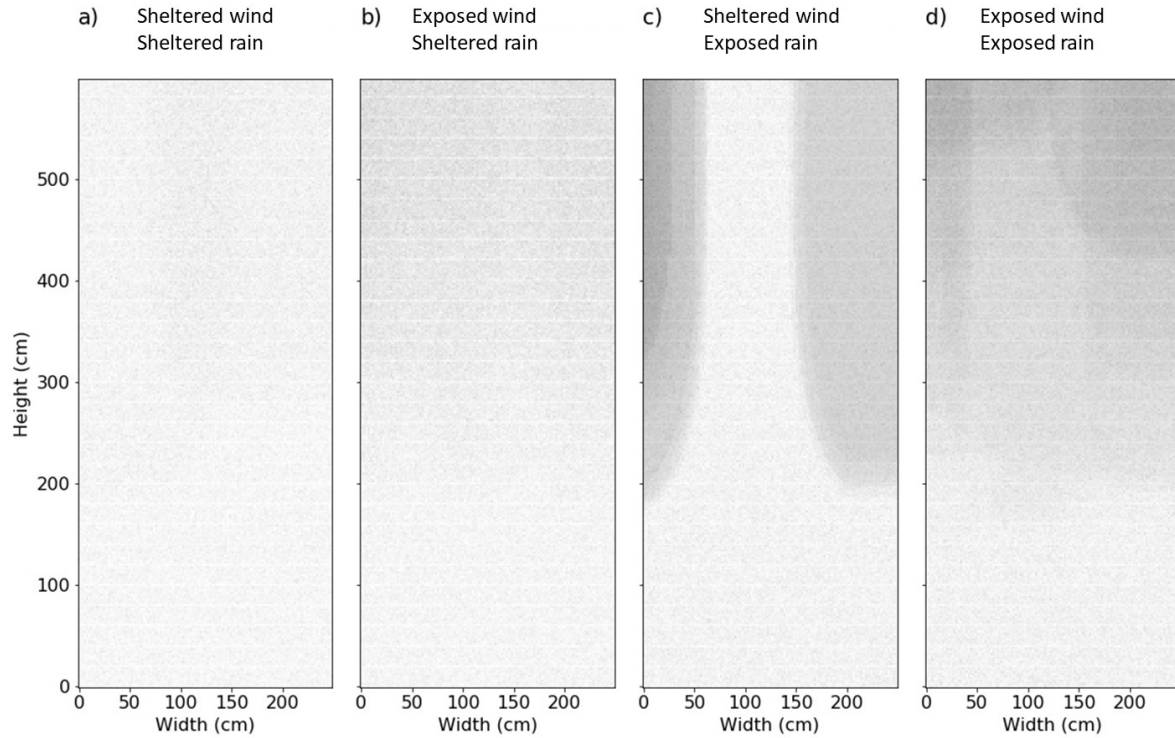


Figure S15: Overall risk of deterioration modelled at 2 cm resolution on walls representing walls in locations a) sheltered from the prevailing wind and sheltered from rainfall, b) exposed to the prevailing wind and sheltered from rainfall, c) sheltered from the prevailing wind and exposed to rainfall and d) exposed to the prevailing wind and exposed to rainfall. Here, sheltered locations are modelled with a mean wind velocity of 5 ms^{-1} and the median rainfall event being 1 mm with an interquartile range of 1.75 mm. Exposed locations modelled with an average wind velocity of 12 ms^{-1} and the median rainfall event being 3 mm with an interquartile range of 8 mm.

316 **S3. Summary**

317 The verification tests showed that ViSTA-HD can:

- 318 • Run simulations using climatic inputs that are representative of those
- 319 occurring at Suoyang;
- 320 • Capture the wind flow and dune dynamics occurring around earthen walls;
- 321 • Capture environmental conditions occurring up a wall face and use these
- 322 conditions to determine the environmental risk of deterioration.

323 **References (additional to manuscript)**

324 Anderson RS, Sørensen M, Willetts BB. 1991. A review of recent progress in our
325 understanding of aeolian sediment transport. In . Springer, Vienna; 1–19.

326 Dong Z, Liu X, Wang H, Wang X. 2003. Aeolian sand transport: a wind tunnel
327 model. *Sedimentary Geology* **161** : 71–83. DOI: 10.1016/S0037-0738(02)00396-
328 2

329 Dupont S, Bergametti G, Marticorena B, Simoëns S. 2013. Modeling saltation
330 intermittency. *Journal of Geophysical Research Atmospheres* **118** : 7109–7128.
331 DOI: 10.1002/jgrd.50528

332 Gares PA, Jackson DWT, Davidson-Arnott RGD, Nordstrom KF, Bauer BO,
333 Sherman DJ, Carter RWG. 1996. Alongshore variations in aeolian sediment
334 transport: Carrick Finn Strand, Ireland. *Journal of Coastal Research* **12** : 673–

335 682.

336 Garvey B, Castro IP, Wiggs G, Bullard J. 2005. Measurements of Flows Over
 337 Isolated Valleys. *Boundary-Layer Meteorology* **117** : 417–446. DOI:
 338 10.1007/s10546-005-2079-6

339 Goossens D, Offer ZY. 2000. Wind tunnel and field calibration of six aeolian dust
 340 samplers. *Atmospheric Environment* **34** : 1043–1057. DOI: 10.1016/S1352-
 341 2310(99)00376-3

342 Li L, Shao M, Wang S, Li Z. 2011. Preservation of earthen heritage sites on the
 343 Silk Road, northwest China from the impact of the environment. *Environmental*
 344 *Earth Sciences* **64** : 1625–1639. DOI: 10.1007/s12665-010-0829-3

345 Mayaud JR, Bailey RM, Wiggs GFS. 2017. A coupled vegetation/sediment
 346 transport model for dryland environments. *Journal of Geophysical Research:*
 347 *Earth Surface* **122** : 875–900. DOI: 10.1002/2016JF004096

348 Richards PJ, Hoxey RP, Short LJ. 2001. Wind pressures on a 6 m cube. *Journal*
 349 *of Wind Engineering and Industrial Aerodynamics* **89** : 1553–1564. DOI:
 350 10.1016/S0167-6105(01)00139-8

351 Rowell ALK, Thomas DSG, Bailey RM, Holmes PJ. 2018. Sand ramps as
 352 palaeoenvironmental archives: Integrating general principles and regional
 353 contexts through reanalysis of the Klipkraal Sands, South Africa. *Geomorphology*
 354 **311** : 103–113. DOI: 10.1016/J.GEOMORPH.2018.03.021

- 355 Shao M, Li L, Wang S, Wang E, Li Z. 2013. Deterioration mechanisms of building
356 materials of Jiaohe ruins in China. *Journal of Cultural Heritage* **14** : 38–44. DOI:
357 10.1016/J.CULHER.2012.03.006
- 358 Sherman DJ, Hotta S. 1990. Aeolian sediment transport: theory and
359 measurement. *Coastal Dunes: form and process* **17** : 16–37.
- 360 Tsoar H. 1983. Wind tunnel modeling of echo and climbing dunes. *Developments*
361 *in Sedimentology* **38** : 247–259. DOI: 10.1016/S0070-4571(08)70798-2
- 362 Tyson S. 1999. Sand ramps or climbing dunes? Identification and
363 palaeoenvironmental significance of aeolian deposits in the southern Kalahari
364 and Breede River Valley, South Africa, University of Cape Town